

# CondiMen: Conditional Multi-Person Mesh Recovery

Romain Brégier\* Fabien Baradel\* Thomas Lucas\* Salma Galaoui\*†

Matthieu Armando\* Philippe Weinzaepfel\* Grégory Rogez\*

\*NAVER LABS Europe

†LIGM, Ecole des Ponts, Univ Gustave Eiffel, CNRS, Marne-la-Vallée, France

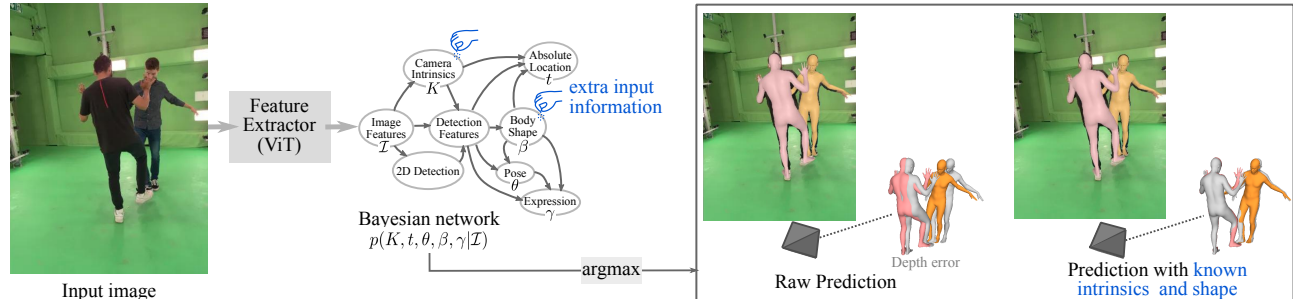


Figure 1: **CondiMen: A Recipe for HMR.** Recovering 3D human meshes from a single image is challenging because predictions can look visually plausible yet be inaccurate in 3D (see second image, where ground-truth meshes are in gray). We propose a method to model such ambiguity and leverage additional information that may be available – such as camera calibration, body shape, distance to the camera, or multi-view observations – to improve predictions (right image). To achieve this, we decompose mesh recovery into a human detection and attribute estimation problem, modeling the joint probability of these attributes (pose, body shape, etc.) using a Bayesian network conditioned on visual features. This approach enables efficient inference, compatible with 20FPS+ real-time applications.

## Abstract

Multi-person human mesh recovery (HMR) consists in detecting all individuals in a given input image, and predicting the body shape, pose, and 3D location for each detected person. The dominant approaches to this task rely on neural networks trained to output a single prediction for each detected individual. In contrast, we propose CondiMen, a method that outputs a joint parametric distribution over likely poses, body shapes, intrinsics and distances to the camera, using a Bayesian network. This approach offers several advantages. First, a probability distribution can handle some inherent ambiguities of this task – such as the uncertainty between a person’s size and their distance to the camera, or simply the loss of information when projecting 3D data onto the 2D image plane. Second, the output distribution can be combined with additional information to produce better predictions, by using *e.g.* known camera or body shape parameters, or by exploiting multi-view observations. Third, one can efficiently extract the most likely predictions from the output distribution, making our proposed approach suitable for real-time applications. Empirically we find that our model i) achieves performance on par with or better than the state-of-the-art, ii) captures uncertainties and correlations inherent in pose estimation and iii) can exploit additional information at test time, such as multi-view consistency or body shape priors. CondiMen spices up the modeling of ambiguity, using just the right ingredients on hand.

## 1. Introduction

Recovering people characteristics in 3D from images is essential for a variety of applications, ranging from human behavior analysis to robotic systems in crowded environments. In this work, we present a method that detects individuals in images and then predicts 3D meshes, encoding their pose, body shape, and location.

Human mesh recovery is an ill-posed problem, as different meshes could be plausible for a single input image

due to factors like clothing, occlusions, and the projective nature of 2D imaging. In particular, the apparent 2D size of a person in an image depends on their actual size in 3D, the distance to the camera, and the camera’s focal length (see supp. mat. for examples). Despite this uncertainty, state-of-the-art methods [4, 32, 63, 64] typically predict deterministic outputs. These methods are optimized to minimize an empirical loss over the training data, and in the presence of ambiguity, they

tend to predict average attributes – those that occur most frequently in the training data – resulting in a loss of accuracy when faced with aleatoric uncertainty.

A probabilistic framework offers an elegant way to handle such uncertainty. Methods that predict probability distributions – allowing for the sampling of hypotheses [35, 36, 44] – or that provide confidence estimates [18, 35, 60] have been proposed in previous work. However, most of them focus solely on relative pose estimation and fail to consider the body shape or 3D location, which are critical in many applications. Moreover, there are scenarios where additional information such as camera calibration, body shapes previously scanned, or multi-view image captures are available and could provide useful cues to improve predictions. Incorporating such external inputs into existing methods is unfortunately challenging and often requires iterative optimization techniques [35], limiting their practical application.

In this paper, we propose a solution to this issue by treating mesh recovery as a task of jointly predicting various attributes (pose, body shape, location, *etc.*), and by regressing a joint probability distribution over these attributes. Specifically, we introduce a parametric Bayesian model [6] illustrated in Fig. 1 that, given an input image, outputs a distribution over camera intrinsics, human detections, poses, body shapes and 3D locations. This probabilistic formulation accounts for task-specific ambiguities and allows for the efficient use of external information during inference. Additionally, multi-view images can seamlessly be used within our framework to improve 3D mesh recovery – something which is not straightforward with monocular deterministic methods. This ability to make multi-view predictions at test time, despite being trained on monocular data only is advantageous because high-quality, diverse monocular data is far more abundant and easier to collect than multi-view data, which often requires complex setups.

For our experiments, we train a model from synthetic-only data, using BEDLAM [7] as well as images we generated to further increase data variability. We demonstrate that the Bayesian nature of our model offers flexibility and the ability to exploit available external knowledge, at test time. For instance, we show that leveraging known ground-truth quantities (*e.g.* camera intrinsics or body shape) within the model can improve predictions in a zero-shot manner. It can also be used to exploit consistency across multiple input images, for instance by enforcing a constant body shape for a given person. We validate the performance of our approach against existing state-of-the-art methods on monocular and multi-view datasets [26, 27, 42, 67, 76], showing

competitive results and the ability to handle uncertainty effectively.

## 2. Related work

**Human Mesh Recovery from a Single Image.** The development of parametric 3D models [41, 48, 73] has advanced the field of human pose estimation from 3D skeleton regression [13, 52, 70] to the prediction of full human body meshes [19, 23, 31, 32, 34, 39, 54, 79]. More recently, research has focused on estimating expressive human meshes [4, 7, 24, 46, 62] and placing these meshes within real-world coordinate systems [59, 68]. The pioneering work by Kanazawa et al. [32] introduces a method to predict SMPL [41] parameters, along with weak-perspective re-projection parameters, from a single cropped image of a person. Subsequent methods have improved on this approach, either by refining the network architecture [23, 39, 79] or by leveraging new training data and protocols [7, 46]. Recent advances have also enabled whole-body pose estimation, *i.e.*, including facial expression and hand poses [11, 15, 21, 24, 40, 43, 47, 53, 80, 84]. A few methods now tackle the detection and regression of multiple human meshes within a single network [4, 51, 62, 63, 64], though these approaches typically produce deterministic outputs. In contrast, our proposed Bayesian network for multi-person whole-body mesh recovery outputs a probability distribution, allowing it to handle ambiguities, integrate external information, and fuse multi-view predictions for more robust performance in complex scenarios.

**Multi-view Human Mesh Recovery** A first category of methods to tackle multi-view mesh recovery assumes known camera calibration to extend single view reconstruction to multi-view settings [8, 16, 82, 85]. In particular, SMPLify-X [8] performs 3D reconstruction in a unified coordinate system by iteratively minimizing 2D keypoint reprojection errors. Some learning-based methods also follow this calibrated approach [14, 28, 65, 74]. For example, Isakov et al. [28] propose a learnable triangulation solution. A second category of methods addresses the uncalibrated setup, where predictions from multiple views are used to estimate camera parameters and merged either through handcrafted averaging [38, 49, 77] or learning-based techniques [50, 85]. Recent adaptive frameworks can handle both calibrated and uncalibrated settings but are still limited to single-person [30, 72]. In contrast, our approach supports multi-person mesh recovery across multiple views.

**Probabilistic Human 3D Pose.** Early methods addressed pose uncertainty through optimization-based formulations [60, 61] or by predicting multiple 3D poses

from 2D cues [29, 36, 81]. Li and Lee [36] use a Mixture Density Network to infer a distribution of 3D joints from 2D joints, while Zhang et al. [81] model separate Gaussian distributions for 2D keypoints and depth. Recent works leverage Normalizing Flow (NF) to model pose or shape probability distributions [35, 37, 58, 69], with Kolotouros et al. [35] conditioning NF on image features to predict SMPL parameters. Another line of research leverages denoising diffusion models [25, 44, 78] that can account for uncertainties in depth, body shape, and camera intrinsics. Extracting the most likely prediction with such approach is often computationally intensive however. Other strategies include using multiple prediction heads with a *best-of-N* loss [5], estimating Gaussian distributions over SMPL parameters [57], or quantizing human mesh representations [22]. Closer to our work, Sengupta et al. [56] use a hierarchical matrix-Fisher distribution for each SMPL rotation parameters following the kinematic tree. We extend this approach by introducing a Bayesian network head that can handle uncertainty while allowing for efficient inference, use of external information, and multi-view predictions in a simple and elegant way.

### 3. Method

We present our method for detecting people and estimating their 3D whole-body attributes from a single input image. This method called *CondiMen* (short for *conditional multi-person mesh recovery*) is illustrated in Fig. 1. We extract image features using a Vision Transformer (ViT) backbone [17], which we use as conditioning variables in a joint probability distribution that models people appearing in the image with their different attributes (3D location, body shape, etc.). We model this joint distribution as a trained Bayesian network. At inference, we efficiently detect humans and predict their attributes, by sequentially extracting modes of the conditional distributions. This probabilistic framework allows us to leverage different information available at inference, such as known camera intrinsics or specific body shapes to enhance prediction accuracy.

#### 3.1. Problem formulation

**Human parametrization.** To encode human meshes, we rely on a parametric body model, namely SMPL-X [15]. SMPL-X provides a whole-body parametrization decoupled into an absolute 3D location  $t$ , a list of bones orientations  $\theta$  modeling the pose, a vector  $\beta$  modeling the body shape and a vector  $\gamma$  modeling the facial expression.

**Bayesian network.** We model the multi-person mesh recovery problem as a probabilistic optimization problem. Given some input image features  $\mathcal{I}$ , we aim at

predicting the value of different random variables: the intrinsic parameters  $K$  of the camera, as well as attributes of people visible in the image  $(t, \theta, \beta, \gamma)$ <sup>1</sup>. We consider the joint probability distribution of these variables conditioned on image features, and aim to extract the most likely prediction:

$$\hat{K}, \hat{t}, \hat{\theta}, \hat{\beta}, \hat{\gamma} = \operatorname{argmax} p(K, t, \theta, \beta, \gamma | \mathcal{I}), \quad (1)$$

where  $p(K, t, \theta, \beta, \gamma | \mathcal{I})$  denotes the associated probability density. While conceptually appealing, modeling such joint distribution from limited data is challenging due to the high dimension of the representation space ( $\dim(K)=3$ ,  $\dim(t)=3$ ,  $\dim(\beta)=11$ ,  $\dim(d)=1$ ,  $\dim(\theta)=53 \times 3$ ,  $\dim(\gamma)=10$  in our setting).

A classical solution to this *curse of dimensionality* is to adopt the naive Bayes assumption, which posits that different variables are conditionally independent given the image features. This results in a factorized form:  $p(K, t, \theta, \beta, \gamma | \mathcal{I}) \approx p(K | \mathcal{I}) \cdot p(t | \mathcal{I}) \cdot p(\theta | \mathcal{I}) \cdot p(\beta | \mathcal{I}) \cdot p(\gamma | \mathcal{I})$ , where  $p(x | y)$  denotes probability density at  $x$  conditioned on the value  $y$ . In practice, each conditional density  $p(\cdot | \mathcal{I})$  is generally assumed to belong to a parametric family, with parameters that are functions of the input  $\mathcal{I}$ , e.g. regressed using a neural network. Multi-HMR [4] and most other deterministic methods [51, 63, 64] can be thought of as special cases within this framework. They use regression objectives equivalent to a naive Bayes formulation, assuming probability distributions with constant dispersion terms. However, a key limitation of the naive Bayes assumption is that it ignores inter-variable dependencies. These dependencies are often crucial for scene understanding: for instance a small person A appearing the same size in 2D as a taller person B is likely to be closer to the camera than B, other things being equal.

To address these challenges, we adopt a relaxed hypothesis by modeling the joint distribution as a Bayesian network, decoupling variables into a directed acyclic graph of conditional distributions, illustrated in Fig. 1. The ability of deep neural networks to model complex, high-dimensional data in an auto-regressive manner has been demonstrated across various domains including text [10, 66] and images [20]. Our Bayesian model is inspired by auto-regressive approaches, encoding relationships between variables in a cascaded fashion.

#### 3.2. Conditional distributions

We implement our Bayesian network using a cascade of Multi-Layer Perceptrons (MLP). Each MLP outputs parameters of a probability distribution associated with a random variable of our mesh recovery problem, such

<sup>1</sup>We consider the single-person case here to simplify notations.

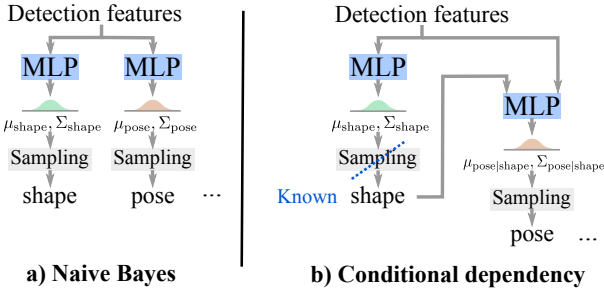


Figure 2: **Modeling conditional dependency.** We predict probability distributions for different human attributes (e.g., pose, shape, distance) and efficiently sample the most likely predictions. Rather than treating each attribute independently (a), we capture their interdependency by modeling conditional distributions (b), leading to more coherent results. Our framework can also incorporate additional input information when available (such as a known shape attribute, shown in blue), to further improve prediction accuracy.

as the pose of a detected person. This distribution is conditioned on the value of its parent variables in the Bayesian network’s graphical model, which allows us to, for example, encode the likelihood of a body pose given a specific body shape and image detection features (see Fig. 1 and Fig. 2). In this section, we present the variables and distributions considered in our experiments.

**Camera intrinsics.** We assume a pinhole camera model with focal length  $f > 0$  and principal point  $p \in \mathbb{R}^2$ . We predict the parameters of Gaussian distributions for  $\ln(f)$  and  $p$ , conditioned on image features, specifically on the [CLS] token output by the ViT image encoder. Considering  $\ln(f)$  instead of  $f$  ensures that  $f > 0$ , and is mathematically equivalent to modeling  $f$  with a log-normal distribution.

**2D detection.** Image features produced by the ViT encoder consist of patch tokens  $P_{u,v}$  defined along a 2D regular grid  $G = \{(u, v)\}_{u=1\dots w, v=1\dots h}$ . We encode people detections as binary variables  $s_{u,v}$  along this grid, which indicate whether a reference keypoint of a person projects into a grid cell  $(u, v) \in G$ , following the CenterNet object detection framework [83]. For each variable, we predict a score  $p(s_{u,v}|\mathcal{I})$  encoding the detection likelihood, which is regressed from the corresponding patch features  $P_{u,v}$ . In practice, we use the person’s head as reference keypoint, assuming that at most one person is detected in each grid cell. At inference, detection is performed via simple score thresholding and local non-maxima suppression.

**Detection features.** For each detected person, we consider a latent variable consisting of image patch features  $P_{u,v}$  of the detected grid cell  $(u, v)$  augmented

with camera ray embeddings, following an approach similar to Multi-HMR [4]. These *detection features* thus depend on camera intrinsics, and will serve as main conditioning variable for predicting the different human attributes.

**Human attributes.** SMPL-X parameterizes body shape and expressions as latent vectors of a PCA space of dimension  $D$  ( $D=11$  for shape,  $D=10$  for expression, in our setup). We therefore model the conditional distributions for shape and expression as multivariate diagonal Gaussians. The absolute 3D location of the person is decomposed into 2D coordinates  $c$  of the reference keypoint in the image, and distance  $d$  to the image plane. To encode this distance, we use the variable  $\ln(d/f)$  referred to as *encoded depth*, and model the conditional distributions for  $c$  and  $\ln(d/f)$  as normal distributions. The  $\ln(d/f)$  encoding ensures that  $d$  remains positive and allows for stronger conditioning on camera intrinsics. Lastly, pose is parameterized as a tuple  $\theta \in SO(3)^J$  of  $J = 53$  bone orientations. Since  $SO(3)$  has a more complex topology than the PCA space of shapes and expressions, we model the conditional pose distribution as a product of independent matrix Fisher distributions  $\prod_{j=1}^J \mathcal{F}(F_j)$  of density defined for a rotation matrix  $R \in SO(3)$  and some distribution parameters  $F \in \mathcal{M}_{3 \times 3}(\mathbb{R})$  by:

$$p_{\mathcal{F}(F)}(R) = c(F) \exp(\text{Tr}(F^T R)), \quad (2)$$

with  $c(F)$  a normalization constant.

**Distribution parametrization.** To model a  $D$ -dimensional Gaussian distribution  $\mathcal{N}(\mu, \Sigma)$  while avoiding degenerate cases, we regress the mode  $\mu \in \mathbb{R}^D$  of the distribution along with dispersion parameters  $\sigma \in \mathbb{R}^D$ , from which we construct the diagonal covariance matrix  $\Sigma = \text{diag}(1 + \exp(\sigma))^2$ . Similarly, we decompose the parameter  $F \in \mathcal{M}_{3 \times 3}(\mathbb{R})$  of a matrix Fisher distribution  $\mathcal{F}(F)$  into a mode  $R \in SO(3)$  and dispersion parameters  $(O \in SO(3), \Lambda \in \mathbb{R}^3)$ , more suitable to be regressed by a MLP. These components are combined as follows:  $F = RO \text{diag}(\lambda \text{sigmoid}(\Lambda))O^T$ , where  $\text{sigmoid}$  denotes the element-wise sigmoid function and  $\lambda$  is a strictly positive scaling constant (we use  $\lambda = 2$  in our experiments). Rotations are regressed as  $3 \times 3$  matrices, which are orthonormalized using a differentiable special Procrustes operator implemented in RoMa [9].

**Normalization constant.** The matrix Fisher probability density function of Eq. (2) is defined up to a constant  $c(F)$ . To evaluate this constant during training, we use numerical integration by sampling 36,864 rotations on a uniform  $SO(3)$  grid proposed by Yerushova et al. [75].



### 3.3. Inference

In many applications, one might be interested in extracting the most likely predictions given observations, *i.e.* the solution of Eq. (1). Finding an optimal solution to this problem is not straightforward, notably due to the non-linearities introduced by the MLPs regressing parameters of our conditional distributions. Fortunately, a greedy but much more efficient alternative exists. This approach consists in considering conditional distributions sequentially, extracting their modes and using them as conditioning value for the downstream distributions of the Bayesian graph in a feed-forward manner. Such algorithm can be implemented very efficiently, as modes are readily available in the parametrization of the normal and Fisher distributions considered. Note that in contrast to our parametric approach, probabilistic models implemented implicitly using normalizing flows [35,58] allow for sampling and estimating probability densities with a forward/backward pass, but they do not admit closed-form solutions for mode extraction.

**Using known variables.** One major advantage of modeling conditional distributions over deterministic regression is the ability to exploit additional information available. In many applications, prior knowledge such as camera intrinsic parameters (from calibration or image metadata), a person’s body shape (when imaging a known individual), or their distance from the camera (using depth sensors, for instance) can be leveraged. At inference, we can use such information as additional input of our Bayesian network, as illustrated Fig. 2b, to improve prediction consistency.

**Multi-view prior.** Better results can be obtained by exploiting  $k$  simultaneous observations of the same person from different viewpoints, when available. In our experiments, we assume that the camera poses are unknown. We decompose the pose parameters into a global rigid orientation parameter  $\theta_0$  and intrinsic, viewpoint-independent, pose parameters  $\tilde{\theta}_j = \theta_0^{-1}\theta_j$ , with  $j = 1 \dots J - 1$ . We then look for the multi-view prediction maximizing the product of posterior probabilities conditioned by image features:

$$\prod_{i=1}^k p(K^i, t^i, (\theta_0^i, \theta_1 \dots \theta_{J-1}), \beta, \gamma | \mathcal{I}^i), \quad (3)$$

where variables specific to a view  $i = 1 \dots k$  are denoted with superscript  $i$ . For greater efficiency, we also solve this problem greedily. We start by an initial rigid alignment of predictions (obtained separately for each view) to estimate global orientations  $(\theta_0^i)_{i=1 \dots k}$ , and then proceed to find the optimal intrinsic orientations  $\tilde{\theta}_j$ . These are determined by minimizing the product of Fisher probability densities  $\prod_{i=1}^k p_{\mathcal{F}(\theta_0^i F_j^i)}(\tilde{\theta}_j)$  for each bone orientation  $j = 1 \dots J - 1$  and view  $i$ , see Eq. (2).

This optimization admits a closed-form solution, which consists for each bone orientation  $\tilde{\theta}_j$  in the special Procrustes orthonormalization of  $\sum_{i=1}^k \theta_0^i F_j^i$ .

**Matching.** With multiple input views and multiple people per view, predictions from each view need to be matched to ensure they correspond to the same person, before they can be combined. For simplicity, we rely on Hungarian matching to obtain these matches, with cost matrices computed from pairs of single-view predictions after rigid alignment.

### 3.4. Training

We train CondiMen to regress conditional distributions using an empirical cross-entropy objective function denoted  $\mathcal{L}_{\text{prob}}$ . This objective function aims to maximize the predicted log-probability density of the ground truth variables  $(K^{*i}, s^{*i}, (t_j^{*i}, \theta_j^{*i}, \beta_j^{*i}, \gamma_j^{*i})_j)$  given images  $i = 1 \dots n$ :

$$\mathcal{L}_{\text{prob}} = -\frac{1}{n} \sum_{i=1}^n \log p(K^{*i}, s^{*i}, (t_j^{*i}, \theta_j^{*i}, \beta_j^{*i}, \gamma_j^{*i})_j | \mathcal{I}^i), \quad (4)$$

with visible people indexed by  $j$ . This joint probability density corresponds to the product of conditional probability densities predicted in our Bayesian network. We minimize the objective function by mini-batch gradient descent.

**Mode guiding.** To achieve better predictions, we found it beneficial to additionally guide the mode extraction procedure of our method. At training time, we consider some input camera intrinsics  $K$  and generate human attribute hypotheses using the procedure described in Sec. 3.3. This results in human mesh predictions  $\hat{V}$ , composed of  $|V|$  vertices centered at 3D location  $\hat{t}$ . Denoting  $\pi_K$  as the 2D projection operator onto the image plane, we aim to minimize an  $L_1$  reprojection error on the vertices relative to the ground truth  $(K^*, V^*, t^*)$ :  $\mathcal{L}_{\text{reproj}} = \frac{1}{|V|} \sum_n |\pi_K(\hat{V}_n + \hat{t}_n) - \pi_{K^*}(V_n^* + t_n^*)|$ . For 50% of the mini-batches, we randomly sample camera intrinsics with an horizontal field-of-view uniformly chosen between 5 and 170°. For the remaining mini-batches, we use ground-truth camera intrinsics, and introduce an additional objective function to minimize an  $L_1$  human-centered vertices loss:  $\mathcal{L}_{\text{mesh}} = \frac{1}{|V|} \sum_n |\hat{V}_n - V_n^*|$ .

With the addition of these two deterministic losses, our total objective function can be expressed as:

$$\mathcal{L} = \mathcal{L}_{\text{prob}} + \mathcal{L}_{\text{mesh}} + \mathcal{L}_{\text{reproj}}. \quad (5)$$

### 3.5. Implementation details

**Architecture.** For our experiments, we use an architecture inspired by the single-shot framework of Multi-HMR [4], for its simplicity and state-of-the-art performance. The input RGB image is encoded via a transformer-based architecture to produce 1024-

dimensional image patch features  $\mathcal{I}$ , alongside detection features of similar dimensions. We train the entire network in an end-to-end manner to minimize the objective function (5), starting from DINOv2 [45] weights initialization for the image encoder. In our default settings, we use a ViT-Large encoder with an image resolution of  $518 \times 518$  and a patch size of  $14 \times 14$ . The MLPs outputting conditional distributions parameters take the conditioning variables as input and combine them through a sum in an hidden space (typically of dimension 256) after linear projection followed by a rectilinear activation. We use the Adam optimizer [33] with a learning rate of  $5 \cdot 10^{-6}$  and train for 500k steps with a batch size of 16 images. We consider all image patches with a detection score above 0.5 as detections in our experiments, after applying a non-maxima suppression of  $3 \times 3$  patch window.

**Training Data.** We train models using only synthetic data in our experiments: synthetic data has the advantage of mitigating personal privacy issues, it provides potentially perfect ground-truth annotations, and was shown to transfer well to real world applications in practice [4, 7, 46]. Namely, we rely on the BEDLAM [7] dataset, which consists of 286k images depicting 951k persons. To further increase the body shape diversity we additionally render a synthetic dataset of 8k scenes. It contains images depicting 7 persons on average, with 40 multi-view renderings per scene, leading to more than 300k images and 2M human instances rendered. Additional details are provided in the supplementary material.

**Computing Resources.** Training our ViT-L model took about 51 hours using one NVIDIA H100 GPU (36h and 35.5 hours resp. for ViT-B and ViT-S variants). Inference time depends on the number of people visible in each image. For reference, we report average inference times on the 3DPW dataset in Table 2a.

## 4. Experiments

To evaluate the effectiveness of our approach, we assess how CondiMen can leverage additional input information, and compare its performance against state-of-the-art methods. We conduct experiments on single-view datasets (3DPW [67] and MuPoTS [42]) as well as multi-view datasets (HI4D [26], Human3.6M [27] and RICH [26]). We report Mean Per Vertex Error in  $mm$ , with or without Procrustes alignment ( $PVE$  and  $PA-PVE$ , resp.), along with mean absolute position error, ( $PE$ ) in  $mm$ . Following previous works [4, 63, 64], we also provide Mean Per Joint Error in  $mm$  ( $PJE$ ) on 3DPW and Human3.6M, and Percentage of Correct Keypoints ( $PCK$ ) within  $15cm$  on MuPoTS. For experiments with additional input information, we convert SMPL anno-

tations of 3DPW to the SMPL-X format using the code from Choutas et al. [15]. Note that we do not perform these experiments on MuPoTS due to the absence of mesh annotations.

**Graph connectivity.** Our Bayesian network architecture introduces conditional dependencies in the estimation of human attributes. For instance, pose prediction depends on body shape, as shown in the graphical model in Fig. 1. To evaluate the effectiveness of this strategy, we compare our approach with a *Naive-Bayes* baseline model, in which human attributes are predicted from detection features independently, without conditional dependencies, as illustrated in Fig. 2. Such baseline is similar to Multi-HMR [4], except that it regresses parametric distributions instead of deterministic values, ensuring a more meaningful comparison with *CondiMen*. Results are summarized in Fig. 3, and additional results can be found in the supp. mat. Our approach consistently outperforms the *Naive-Bayes* baseline, especially when leveraging additional input information for certain variables. This result underscores the importance of modeling dependencies between human attributes.

**Additional input information.** We report in Fig. 3 performance gains achieved when incorporating additional input information, using the approach described in Sec. 3.3. As expected, providing distance to the camera in addition to the camera intrinsics (*intrinsics-distance*) significantly enhances mean absolute vertex position accuracy, reducing the average PE error across datasets to 91mm for *CondiMen* and 103mm for *Naive Bayes*. Exploiting body shape information similarly boosts relative pose estimation, yielding up to a 25% reduction in PVE error. It also brings significant improvement in term of absolute position error (-57% on HI4D, -57% on RICH for *CondiMen*), which suggests that the model is able to capture the relationship between visual appearance, body shape and distance to the camera, and to exploit this dependency to produce better predictions (see examples Fig. 1 and 4). In contrast, the *Naive Bayes* baseline which does not model attribute interdependencies shows only minor improvements in absolute position error (-1.6% HI4D and -0.5% on RICH). On 3DPW, using additional shape information has marginal impact, as the model’s initial shape estimates are already rather close to ground truth. However, using camera intrinsics significantly reduces localization error (by 53% between *none* and *intrinsics*). Finally, incorporating external information regarding camera intrinsics, body shape and distance to the camera provides further improvements for both methods.

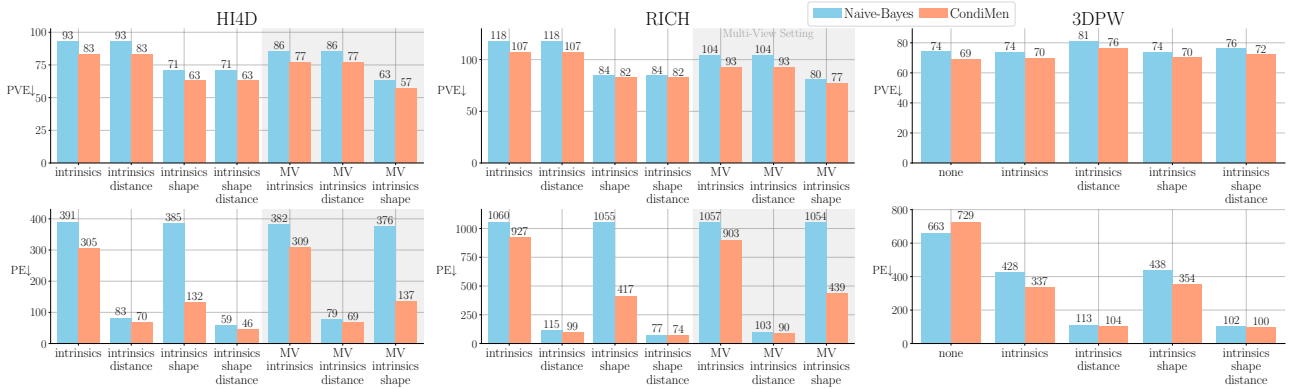


Figure 3: **Impact of additional information.** We report metrics for mesh reconstruction accuracy (Per Vertex Error, PVE) and 3D positioning (Positioning Error, PE) across different datasets. Exploiting additional information such as camera intrinsics (*intrinsics*), body shape parameters (*shape*), distance to the camera (*distance*), or multi-view observations (MV) can significantly reduce prediction errors. By modeling relationships between variables, *CondiMen* can consistently achieve lower errors than a *Naive Bayes* baseline.

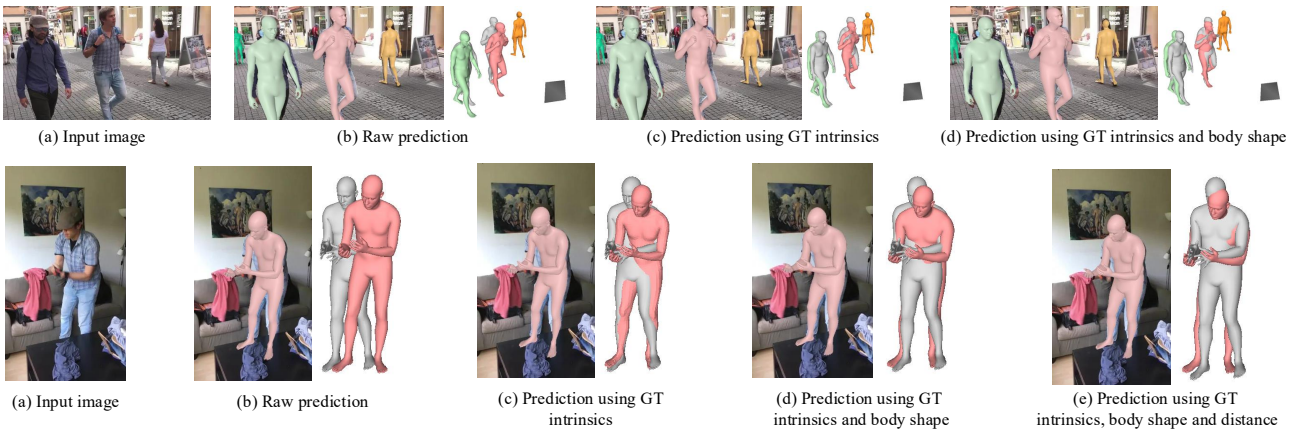


Figure 4: **Qualitative results.** Leveraging additional inputs, such as camera intrinsics and body shape, reduces errors and improves mesh accuracy. Ground-truth meshes are shown in grey for comparison.

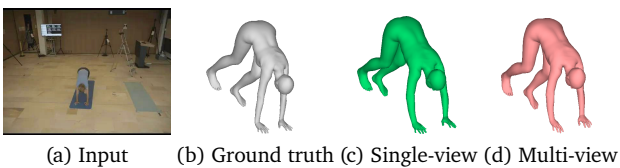


Figure 5: **Improved prediction using multi-view prior.**

**Multi-view.** We also report in Fig. 3 results obtained using a multi-view consistency prior, using the approach described in Sec. 3.3. We observe that the use of multiple views results in a smaller PVE error compared to the monocular case (see also Fig 5), and that providing external input leads to further performance improvements, with observations similar to the ones made in the monocular case.

**State-of-the-art comparison.** Finally, we compare the performance of our proposed method with recent approaches in both monocular and multi-view settings. Table 1 presents the performance results as reported

by the authors, except for Multi-HMR [4], which we retrained on our dataset using a ViT-Large backbone at 518×518 resolution for a fair comparison. Following established practices [85], we report our results for Human3.6M, HI4D and RICH after fine-tuning *CondiMen* on each dataset for 15k steps, and we use ground-truth camera intrinsics for evaluation [4]. We also report results of a strong multi-view baseline – denoted *Multi-HMR+avg* which averages (after a rigid registration) the shape and expression vectors, as well as the absolute bone orientations predicted by Multi-HMR across multiple views. *CondiMen* achieves highly competitive results in both monocular and multi-view settings, and we provide qualitative examples in Fig. 4 and 6.

#### 4.1. Additional ablations

**Backbone.** Tab. 2a shows the results when experimenting with various image encoder backbones. As expected, larger backbones yield better results: a ViT-





Figure 6: **Qualitative results** CondiMen’s raw predictions remain accurate even when no additional data, such as camera intrinsics or body shape, is available in the wild. Here, for instance, on examples from the MuPoTS dataset.

Method	MV	Human3.6M ↓				HI4D ↓	
		PJE	PA-PJE	PVE	PA-PVE	PVE	PA-PVE
ProHMR [35]		65.1	43.7	–	–	–	–
ROMP [63]		–	–	–	–	215.3	–
BEV [64]		–	–	–	–	153.9	–
HMR2.0 [23]		<u>50.0</u>	<b>32.4</b>	–	–	141.2	–
Yu et al. [77]		–	41.6	–	46.4	–	–
SMPLer-X[11]		–	<u>38.9</u>	–	42.8	–	–
MUC [85]		–	44.3	–	45.8	–	–
Multi-HMR [4]		50.8	40.0	<u>62.2</u>	<u>43.3</u>	<u>49.0</u>	<u>36.2</u>
<b>Ours</b>		<b>49.0</b>	<u>38.9</u>	<b>59.1</b>	<b>42.2</b>	<b>48.8</b>	<b>35.7</b>

ProHMR [35]	✓	62.2	34.5	–	–	–	–
Yu et al. [77]	✓	–	33.0	–	<u>34.4</u>	–	–
SMPLer-X[11] + avg	✓	–	33.4	–	37.1	–	–
MUC [85]	✓	–	31.9	–	33.4	–	–
Calib-free PaFF [30]	✓	44.8	<u>28.2</u>	–	–	–	–
OVR [72]	✓	–	<b>27.1</b>	–	<b>28.9</b>	–	–
Multi-HMR [4] + avg	✓	<u>42.8</u>	30.0	51.3	32.5	<u>51.1</u>	<u>28.7</u>
<b>Ours</b>	✓	<b>41.1</b>	28.9	<b>49.0</b>	<u>31.2</u>	<b>44.7</b>	<b>27.8</b>

(a) Multi-view setting.

Method	MV	Whole-body ↓		Hands ↓	Face ↓
		PVE	PA-PVE	PA-PVE	PA-PVE
MUC [85]		–	47.7	8.2	4.1
Multi-HMR [4]		<u>69.4</u>	<u>38.2</u>	<u>7.4</u>	<u>3.7</u>
<b>Ours</b>		<b>65.4</b>	<b>36.5</b>	<b>7.3</b>	<b>3.6</b>

MUC [85]	✓	–	33.5	<b>6.7</b>	<b>3.2</b>
Multi-HMR [4] + avg	✓	61.7	29.5	6.8	3.5
<b>Ours</b>	✓	<b>57.8</b>	<b>27.9</b>	<b>6.7</b>	<b>3.4</b>

(b) Body-part specific results on RICH.

Method	3DPW ↓		MuPoTS PCK ↑	
	PJE	PA-PJE	Matched	All
ProHMR [35]	–	59.8	–	–
ROMP [63]	76.7	47.3	69.9	72.2
BEV [64]	78.5	46.9	75.2	70.2
Multi-HMR [4]	70.6	47.5	<u>77.6</u>	<b>82.7</b>
HMR2.0 [23]	81.3	54.3	–	–
POCO [18]	<u>69.7</u>	<u>42.8</u>	–	–
<b>Ours</b>	<b>69.5</b>	<b>46.4</b>	<b>84.7</b>	<u>74.0</u>

(c) Monocular setting.

Table 1: Comparison with state-of-the-art methods in monocular and multi-view settings.

Large model performs better than a ViT-Base which itself performs better than ViT-Small, likely due to the large scale of the training sets. However, these improvements in prediction quality come with additional computation costs both at training and inference time. Still, inference takes less than 50ms per image on average with a ViT-Large backbone, making it suitable for some real-time applications.

**Training procedure.** We also conduct ablation studies on various aspects of our training procedure, with results presented in Table 2b. First, we remove the mode-guiding objectives described in Sec. 3.4 and observe a drop in performance across all datasets. We also train a variant of our model without the additional synthetic data we generated. While this variant performs better on Human3.6M and HI4D, its performance is

worse on RICH, 3DPW, and MuPoTS. We posit this is due to the presence of less standard camera parameters or body shape attributes in these benchmarks, for which the diversity of additional training data proves beneficial.

**Uncertainty modeling** Empirically, we observe a correlation between the predicted likelihood  $p(K, t, \theta, \beta, \gamma | I)$  and the prediction errors (see supp. mat.). This suggests that the proposed model is able to estimate prediction uncertainty to some extent, an information that could be valuable for downstream applications.

## 5. Discussion

We propose a novel approach for multi-person human mesh recovery, based on a Bayesian network. This



Backbone	Human3.6M↓	HI4D↓	RICH↓	3DPW↓	MuPoTS↑	Inference↓ (ms)
ViT-Small	117.9	96.2	114.2	83.2	67.8	21
ViT-Base	99.7	93.3	108.2	76.6	69.7	25
ViT-Large	<b>88.8</b>	<b>77.0</b>	<b>92.8</b>	<b>69.5</b>	<b>74.0</b>	47

(a) Backbone size.

Training	Human3.6M↓	HI4D↓	RICH↓	3DPW↓	MuPoTS↑
<b>Ours</b>	88.8	77.0	<b>92.8</b>	<b>69.5</b>	<b>74.0</b>
w/o mode guiding	92.4	78.5	106.1	75.3	71.8
w/o additional synth. data	<b>75.9</b>	<b>73.8</b>	96.4	74.4	71.5

(b) Training.

Table 2: **Ablation study.** We report PVE metric in a multi-view setting on Human3.6M, HI4D and RICH. We report PJE for 3DPW and PCK-All for MuPoTS in a monocular setting. Inference durations are measured with an NVidia H100 GPU.

method enables the seamless incorporation of additional input information – such as camera intrinsics, body shape, distance from the camera, or even multi-view acquisitions – to improve the predictions. We believe this has a significant practical value, as such data is readily available in many real-world applications. Our approach achieves on par or better performances than existing state-of-the-art methods on standard benchmarks, while still maintaining real-time capabilities. The motivation behind our work was to exploit interdependencies between various attributes in the mesh recovery problem (e.g. detection, camera parameters, and pose estimation). To this end, we adopted a Bayesian network framework, which is conceptually simple and supports highly efficient inference. Our findings confirm the effectiveness of this approach and suggest that exploring more sophisticated probabilistic modeling techniques could be a promising direction for future research.

## References

- [1] Blender. <https://www.blender.org/>. 13
- [2] Humgen3d. <https://www.humgen3d.com/>. 13
- [3] Poly haven. <https://polyhaven.com/>. 13
- [4] Fabien Baradel, Matthieu Armando, Salma Galaoui, Romain Brégier, Philippe Weinzaepfel, Grégory Rogez, and Thomas Lucas. Multi-hmr: Multi-person whole-body human mesh recovery in a single shot. In *ECCV*, 2024. 1, 2, 3, 4, 5, 6, 7, 8
- [5] Benjamin Biggs, David Novotny, Sebastien Ehrhardt, Hanbyul Joo, Ben Graham, and Andrea Vedaldi. 3d multi-bodies: Fitting sets of plausible 3d human models to ambiguous image data. In *NeurIPS*, 2020. 3
- [6] Christopher M Bishop and Nasser M Nasrabadi. *Pattern recognition and machine learning*. Springer, 2006. 2
- [7] Michael J Black, Priyanka Patel, Joachim Tesch, and Jinlong Yang. Bedlam: A synthetic dataset of bodies exhibiting detailed lifelike animated motion. In *CVPR*, 2023. 2, 6, 18
- [8] Federica Bogo, Angjoo Kanazawa, Christoph Lassner, Peter Gehler, Javier Romero, and Michael J Black. Keep it smpl: Automatic estimation of 3d human pose and shape from a single image. In *ECCV*, 2016. 2
- [9] Romain Brégier. Deep regression on manifolds: a 3D rotation case study. In *3DV*, 2021. 4
- [10] Tom Brown, Benjamin Mann, Nick Ryder, Melanie Subbiah, Jared D Kaplan, Prafulla Dhariwal, Arvind Nee-lakantan, Pranav Shyam, Girish Sastry, Amanda Askell, et al. Language models are few-shot learners. In *NeurIPS*, 2020. 3
- [11] Zhongang Cai, Wanqi Yin, Ailing Zeng, Chen Wei, Qingping Sun, Yanjun Wang, Hui En Pang, Haiyi Mei, Mingyuan Zhang, Lei Zhang, et al. Smpler-x: Scaling up expressive human pose and shape estimation. In *NeurIPS*, 2023. 2, 8
- [12] Angel Chang, Angela Dai, Thomas Funkhouser, Maciej Halber, Matthias Niessner, Manolis Savva, Shuran Song, Andy Zeng, and Yinda Zhang. Matterport3D: Learning from RGB-D data in indoor environments. In *3DV*, 2017. 13
- [13] Wenzheng Chen, Huan Wang, Yangyan Li, Hao Su, Zhenhua Wang, Changhe Tu, Dani Lischinski, Daniel Cohen-Or, and Baoquan Chen. Synthesizing training images for boosting human 3d pose estimation. In *3DV*, 2016. 2
- [14] Rohan Choudhury, Kris M Kitani, and László A Jeni. Tempo: Efficient multi-view pose estimation, tracking, and forecasting. In *ICCV*, 2023. 2
- [15] Vasileios Choutas, Georgios Pavlakos, Timo Bolkart, Dimitrios Tzionas, and Michael J Black. Monocular expressive body regression through body-driven attention. In *ECCV*, 2020. 2, 3, 6
- [16] Vandad Davoodnia, Saeed Ghorbani, Marc-André Carbonneau, Alexandre Messier, and Ali Etemad. Up-ose3d: Uncertainty-aware 3d human pose estimation with cross-view and temporal cues. In *ECCV*, 2024. 2
- [17] Alexey Dosovitskiy, Lucas Beyer, Alexander Kolesnikov, Dirk Weissenborn, Xiaohua Zhai, Thomas Unterthiner, Mostafa Dehghani, Matthias Minderer, Georg Heigold, Sylvain Gelly, et al. An image is worth 16x16 words: Transformers for image recognition at scale. In *ICLR*, 2021. 3
- [18] Sai Kumar Dwivedi, Cordelia Schmid, Hongwei Yi, Michael J Black, and Dimitrios Tzionas. Poco: 3d pose and shape estimation with confidence. In *3DV*, 2024. 2, 8
- [19] Sai Kumar Dwivedi, Yu Sun, Priyanka Patel, Yao Feng, and Michael J Black. Tokenhmr: Advancing human mesh recovery with a tokenized pose representation. In *CVPR*, 2024. 2
- [20] Patrick Esser, Robin Rombach, and Bjorn Ommer. Tam-ing transformers for high-resolution image synthesis. In *CVPR*, 2021. 3

- 
- [21] Yao Feng, Vasileios Choutas, Timo Bolkart, Dimitrios Tzionas, and Michael J Black. Collaborative regression of expressive bodies using moderation. In *3DV*, 2021. 2
- [22] Guéno le Fiche, Simon Leglaive, Xavier Alameda-Pineda, Antonio Agudo, and Francesc Moreno-Noguer. Vq-hps: Human pose and shape estimation in a vector-quantized latent space. *ECCV*, 2024. 3
- [23] Shubham Goel, Georgios Pavlakos, Jathushan Rajasegaran, Angjoo Kanazawa, and Jitendra Malik. Humans in 4d: Reconstructing and tracking humans with transformers. In *ICCV*, 2023. 2, 8
- [24] Charlie Hewitt, Fatemeh Saleh, Sadegh Aliakbarian, Lohit Petikam, Shideh Rezaeifar, Louis Florentin, Zafirah Hosenie, Thomas J Cashman, Julien Valentin, Darren Cosker, et al. Look ma, no markers: holistic performance capture without the hassle. In *SIGGRAPH Asia*, 2024. 2
- [25] Buzhen Huang, Chen Li, Chongyang Xu, Liang Pan, Yang Wang, and Gim Hee Lee. Closely interactive human reconstruction with proxemics and physics-guided adaptation. In *CVPR*, 2024. 3
- [26] Chun-Hao P. Huang, Hongwei Yi, Markus H oschle, Matvey Safroshkin, Tsvetelina Alexiadis, Senya Polikovsky, Daniel Scharstein, and Michael J. Black. Capturing and inferring dense full-body human-scene contact. In *CVPR*, 2022. 2, 6
- [27] Catalin Ionescu, Dragos Papava, Vlad Olaru, and Cristian Sminchisescu. Human3.6m: Large scale datasets and predictive methods for 3d human sensing in natural environments. *IEEE Trans. PAMI*, 2014. 2, 6
- [28] Karim Isakov, Egor Burkov, Victor Lempitsky, and Yuriy Malkov. Learnable triangulation of human pose. In *ICCV*, 2019. 2
- [29] Ehsan Jahangiri and Alan L Yuille. Generating multiple diverse hypotheses for human 3d pose consistent with 2d joint detections. In *ICCVW*, 2017. 3
- [30] Kai Jia, Hongwen Zhang, Liang An, and Yebin Liu. Delving deep into pixel alignment feature for accurate multi-view human mesh recovery. In *AAAI*, 2023. 2, 8
- [31] Hanbyul Joo, Natalia Neverova, and Andrea Vedaldi. Exemplar fine-tuning for 3d human model fitting towards in-the-wild 3d human pose estimation. In *3DV*, 2021. 2
- [32] Angjoo Kanazawa, Michael J. Black, David W. Jacobs, and Jitendra Malik. End-to-end recovery of human shape and pose. In *CVPR*, 2018. 1, 2
- [33] Diederik P. Kingma and Jimmy Ba. Adam: A method for stochastic optimization. In *ICLR*, 2015. 6
- [34] Nikos Kolotouros, Georgios Pavlakos, Michael J Black, and Kostas Daniilidis. Learning to reconstruct 3d human pose and shape via model-fitting in the loop. In *ICCV*, 2019. 2
- [35] Nikos Kolotouros, Georgios Pavlakos, Dinesh Jayaraman, and Kostas Daniilidis. Probabilistic modeling for human mesh recovery. In *ICCV*, 2021. 2, 3, 5, 8
- [36] Chen Li and Gim Hee Lee. Generating multiple hypotheses for 3d human pose estimation with mixture density network. In *CVPR*, 2019. 2, 3
- [37] Jiefeng Li, Siyuan Bian, Ailing Zeng, Can Wang, Bo Pang, Wentao Liu, and Cewu Lu. Human pose regression with residual log-likelihood estimation. In *ICCV*, 2021. 3
- [38] Zhongguo Li, Magnus Oskarsson, and Anders Heyden. 3d human pose and shape estimation through collaborative learning and multi-view model-fitting. In *WACV*, 2021. 2
- [39] Zhihao Li, Jianzhuang Liu, Zhensong Zhang, Songcen Xu, and Youliang Yan. Cliff: Carrying location information in full frames into human pose and shape estimation. In *ECCV*, 2022. 2
- [40] Jing Lin, Ailing Zeng, Haoqian Wang, Lei Zhang, and Yu Li. One-stage 3d whole-body mesh recovery with component aware transformer. In *CVPR*, 2023. 2
- [41] Matthew Loper, Naureen Mahmood, Javier Romero, Gerard Pons-Moll, and Michael J. Black. SMPL: A skinned multi-person linear model. *ACM Trans. Graphics*, 2015. 2
- [42] Dushyant Mehta, Oleksandr Sotnychenko, Franziska Mueller, Weipeng Xu, Srinath Sridhar, Gerard Pons-Moll, and Christian Theobalt. Single-shot multi-person 3d pose estimation from monocular rgb. In *3DV*, 2018. 2, 6
- [43] Gyeongsik Moon, Hongsuk Choi, and Kyoung Mu Lee. Accurate 3d hand pose estimation for whole-body 3d human mesh estimation. In *CVPRW*, 2022. 2
- [44] Lea M uller, Vickie Ye, Georgios Pavlakos, Michael Black, and Angjoo Kanazawa. Generative Proxemics: A Prior for 3D Social Interaction from Images. In *CVPR*, 2024. 2, 3
- [45] Maxime Oquab, Timoth e Darcet, Th eo Moutakanni, Huy Vo, Marc Szafraniec, Vasil Khalidov, Pierre Fernandez, Daniel Haziza, Francisco Massa, Alaaeldin El-Nouby, et al. DINOv2: Learning robust visual features without supervision. *TMLR*, 2024. 6
- [46] Priyanka Patel, Chun-Hao P Huang, Joachim Tesch, David T Hoffmann, Shashank Tripathi, and Michael J Black. Agora: Avatars in geography optimized for regression analysis. In *CVPR*, 2021. 2, 6
- [47] Georgios Pavlakos, Vasileios Choutas, Nima Ghorbani, Timo Bolkart, Ahmed AA Osman, Dimitrios Tzionas, and Michael J Black. Expressive body capture: 3d hands, face, and body from a single image. In *CVPR*, 2019. 2
- [48] Georgios Pavlakos, Vasileios Choutas, Nima Ghorbani, Timo Bolkart, Ahmed AA Osman, Dimitrios Tzionas, and Michael J Black. Expressive body capture: 3d hands, face, and body from a single image. In *CVPR*, 2019. 2
- [49] Georgios Pavlakos, Jitendra Malik, and Angjoo Kanazawa. Human mesh recovery from multiple shots. In *CVPR*, 2022. 2
- [50] Haibo Qiu, Chunyu Wang, Jingdong Wang, Naiyan Wang, and Wenjun Zeng. Cross view fusion for 3d human pose estimation. In *ICCV*, 2019. 2
- [51] Zhongwei Qiu, Qiansheng Yang, Jian Wang, Haocheng Feng, Junyu Han, Errui Ding, Chang Xu, Dongmei Fu, and Jingdong Wang. Psvt: End-to-end multi-person
-

- 3d pose and shape estimation with progressive video transformers. In *CVPR*, 2023. 2, 3
- [52] Gregory Rogez, Philippe Weinzaepfel, and Cordelia Schmid. Lcr-net: Localization-classification-regression for human pose. In *CVPR*, 2017. 2
- [53] Yu Rong, Takaaki Shiratori, and Hanbyul Joo. Frankmocap: A monocular 3d whole-body pose estimation system via regression and integration. In *ICCV*, 2021. 2
- [54] István Sáráncsi and Gerard Pons-Moll. Neural localizer fields for continuous 3d human pose and shape estimation. *NeurIPS*, 2024. 2
- [55] Manolis Savva, Abhishek Kadian, Oleksandr Maksymets, Yili Zhao, Erik Wijmans, Bhavana Jain, Julian Straub, Jia Liu, Vladlen Koltun, Jitendra Malik, et al. Habitat: A platform for embodied ai research. In *ICCV*, 2019. 13
- [56] Akash Sengupta, Ignas Budvytis, and Roberto Cipolla. Hierarchical kinematic probability distributions for 3d human shape and pose estimation from images in the wild. In *ICCV*, 2021. 3
- [57] Akash Sengupta, Ignas Budvytis, and Roberto Cipolla. Probabilistic 3d human shape and pose estimation from multiple unconstrained images in the wild. In *CVPR*, 2021. 3
- [58] Akash Sengupta, Ignas Budvytis, and Roberto Cipolla. Humaniflow: Ancestor-conditioned normalising flows on so (3) manifolds for human pose and shape distribution estimation. In *CVPR*, 2023. 3, 5
- [59] Soyong Shin, Juyong Kim, Eni Halilaj, and Michael J Black. Wham: Reconstructing world-grounded humans with accurate 3d motion. In *CVPR*, 2024. 2
- [60] Hedvig Sidenbladh, Michael J Black, and David J Fleet. Stochastic tracking of 3d human figures using 2d image motion. In *ECCV*, 2000. 2
- [61] Cristian Sminchisescu and Bill Triggs. Covariance scaled sampling for monocular 3d body tracking. In *CVPR*, 2001. 2
- [62] Qingping Sun, Yanjun Wang, Ailing Zeng, Wanqi Yin, Chen Wei, Wenjia Wang, Haiyi Mei, Chi-Sing Leung, Ziwei Liu, Lei Yang, et al. Aios: All-in-one-stage expressive human pose and shape estimation. In *CVPR*, 2024. 2
- [63] Yu Sun, Qian Bao, Wu Liu, Yili Fu, Michael J Black, and Tao Mei. Monocular, one-stage, regression of multiple 3d people. In *ICCV*, 2021. 1, 2, 3, 6, 8
- [64] Yu Sun, Wu Liu, Qian Bao, Yili Fu, Tao Mei, and Michael J Black. Putting people in their place: Monocular regression of 3d people in depth. In *CVPR*, 2022. 1, 2, 3, 6, 8
- [65] Hanyue Tu, Chunyu Wang, and Wenjun Zeng. Voxelpose: Towards multi-camera 3d human pose estimation in wild environment. In *ECCV*, 2020. 2
- [66] Aaron Van den Oord, Nal Kalchbrenner, Lasse Espeholt, Oriol Vinyals, Alex Graves, et al. Conditional image generation with pixelcnn decoders. In *NeurIPS*, 2016. 3
- [67] Timo von Marcard, Roberto Henschel, Michael J. Black, Bodo Rosenhahn, and Gerard Pons-Moll. Recovering accurate 3d human pose in the wild using imus and a moving camera. In *ECCV*, 2018. 2, 6
- [68] Yufu Wang, Ziyun Wang, Lingjie Liu, and Kostas Daniilidis. Tram: Global trajectory and motion of 3d humans from in-the-wild videos. In *ECCV*, 2024. 2
- [69] Tom Wehrbein, Marco Rudolph, Bodo Rosenhahn, and Bastian Wandt. Probabilistic monocular 3d human pose estimation with normalizing flows. In *ICCV*, 2021. 3
- [70] Philippe Weinzaepfel, Romain Brégier, Hadrien Combaluzier, Vincent Leroy, and Grégory Rogez. Dope: Distillation of part experts for whole-body 3d pose estimation in the wild. In *ECCV*, 2020. 2
- [71] Fei Xia, Amir R. Zamir, Zhi-Yang He, Alexander Sax, Jitendra Malik, and Silvio Savarese. Gibson Env: real-world perception for embodied agents. In *CVPR*, 2018. 13
- [72] Zhenyu Xie, Huanyu He, Gui Zou, Jie Wu, Guoliang Liu, Jun Zhao, Yingxue Wang, Hui Lin, and Weiyao Lin. Visibility-guided human body reconstruction from uncalibrated multi-view cameras. In *ICMR*, 2024. 2, 8
- [73] Hongyi Xu, Eduard Gabriel Bazavan, Andrei Zanfir, William T Freeman, Rahul Sukthankar, and Cristian Sminchisescu. Ghum & ghuml: Generative 3d human shape and articulated pose models. In *CVPR*, 2020. 2
- [74] Hang Ye, Wentao Zhu, Chunyu Wang, Rujie Wu, and Yizhou Wang. Faster voxelpose: Real-time 3d human pose estimation by orthographic projection. In *ECCV*, 2022. 2
- [75] Anna Yershova, Swati Jain, Steven M Lavalley, and Julie C Mitchell. Generating uniform incremental grids on so (3) using the hopf fibration. *IJRR*, 2010. 4
- [76] Yifei Yin, Chen Guo, Manuel Kaufmann, Juan Zarate, Jie Song, and Otmar Hilliges. Hi4d: 4d instance segmentation of close human interaction. In *CVPR*, 2023. 2
- [77] Zhixuan Yu, Linguang Zhang, Yuanlu Xu, Chengcheng Tang, Luan Tran, Cem Keskin, and Hyun Soo Park. Multiview human body reconstruction from uncalibrated cameras. In *NeurIPS*, 2022. 2, 8
- [78] Ye Yuan, Jiaming Song, Umar Iqbal, Arash Vahdat, and Jan Kautz. Physdiff: Physics-guided human motion diffusion model. In *ICCV*, 2023. 3
- [79] Hongwen Zhang, Yating Tian, Xinchu Zhou, Wanli Ouyang, Yebin Liu, Limin Wang, and Zhenan Sun. Pymaf: 3d human pose and shape regression with pyramidal mesh alignment feedback loop. In *ICCV*, 2021. 2
- [80] Hongwen Zhang, Yating Tian, Yuxiang Zhang, Mengcheng Li, Liang An, Zhenan Sun, and Yebin Liu. Pymaf-x: Towards well-aligned full-body model regression from monocular images. *IEEE Trans. PAMI*, 2023. 2
- [81] Jinlu Zhang, Yujin Chen, and Zhigang Tu. Uncertainty-aware 3d human pose estimation from monocular video. In *ACMMM*, 2022. 3
- [82] Siwei Zhang, Qianli Ma, Yan Zhang, Sadegh Aliakbarian, Darren Cosker, and Siyu Tang. Probabilistic human

- mesh recovery in 3d scenes from egocentric views. In *ICCV*, 2023. [2](#)
- [83] Xingyi Zhou, Dequan Wang, and Philipp Krähenbühl. Objects as points. In *arXiv preprint arXiv:1904.07850*, 2019. [4](#)
- [84] Yuxiao Zhou, Marc Habermann, Ikhsanul Habibie, Ayush Tewari, Christian Theobalt, and Feng Xu. Monocular real-time full body capture with inter-part correlations. In *CVPR*, 2021. [2](#)
- [85] Yitao Zhu, Sheng Wang, Mengjie Xu, Zixu Zhuang, Zhixin Wang, Kaidong Wang, Han Zhang, and Qian Wang. Muc: Mixture of uncalibrated cameras for robust 3d human body reconstruction. *arXiv preprint arXiv:2403.05055*, 2024. [2](#), [7](#), [8](#)



## Supplementary material

This document provides additional material regarding *CondiMen: Conditional Multi-Person Mesh Recovery*. In Sec. A, B and C we report results of additional experiments aiming at better characterizing properties of CondiMen. Sec. D contains experimental results considering different Bayesian network connectivity, complementing results presented in the main paper. Lastly, in Sec. E we describe some implementation details used in our experiments.

### A. Attributes dependency modeling

In addition to the numerical results reported in the main paper, Fig. 7 provides qualitative results of counterfactual experiments that illustrate the ability of our approach to model dependencies between attributes in the mesh recovery problem. In Fig. 7a, we vary the principal component of body shape parameters (as external inputs) while keeping camera intrinsics constant, and observe the effect on predicted distances to the camera. Similarly, Fig. 7b illustrates the effect of setting different focal lengths as inputs, demonstrating how this variation influences other variables, particularly the distance to the camera.

### B. Uncertainty modeling

Empirically, we observe a correlation between the conditional likelihoods of our predictions – *i.e.* the value of conditional probability densities predicted by our Bayesian network – and actual prediction errors, as illustrated in Fig. 8 for various test sets. This suggests that the proposed model is able to capture the uncertainty of its predictions to some extent, which could be useful in downstream applications.

### C. In-the-wild mesh recovery results

We present CondiMen results on in-the-wild images downloaded from [pexels.com](https://pexels.com) in Fig. 9 and 10. Overall, CondiMen produces highly plausible predictions. However, it also inherits common limitations of existing mesh recovery methods. Notable failure cases (not specific to our method) include unusual poses that deviate significantly from the training data (Fig. 10 top row). Additionally, scenes with mutually occluding persons introduce ambiguity in the detection task (Fig. 10 bottom row).

### D. Bayesian network connectivity

Beyond *CondiMen* and the *Naive Bayes* baseline presented in the main paper, we also experimented with two additional variants to study the impact of

Bayesian network connectivity on numerical performances. Fig. 11 shows the full connectivity of the different Bayesian networks considered in this study, from which the graphical model Fig. 1 of the main paper is extracted. *Variant1* features a denser set of conditional dependency connections compared to *CondiMen*, and in *Variant2* the dependency order between body shape and encoded depth variables is furthermore permuted. We report results of quantitative evaluations in Table 3. The dependency order in *Variant2* prevents from properly exploiting external camera intrinsics and body shape inputs, leading to much larger absolute position errors in this setting than with *CondiMen* and *Variant1*, but still outperforming the *Naive Bayes* baseline (*e.g.* on *Human3.6M* in *Single-View intr-shape* setup,  $PE = 676.9mm$  for *Variant2* vs.  $284.6mm$  for *CondiMen*,  $366.2mm$  for *Variant1*, and  $898.0mm$  for *Naive Bayes*). Overall, *CondiMen* achieves better numerical performances than *Variant1*. The restricted connectivity of *CondiMen* imposes stronger inductive biases than the connectivity of *Variant1*, and we posit it helps learning meaningful correlations between human attributes. This observation is arguably dependent of our training strategy, and we expect that further increasing the amount and variability of training data would diminish the benefits of imposing such inductive priors.

### E. Implementation details

#### E.1. Additional synthetic data

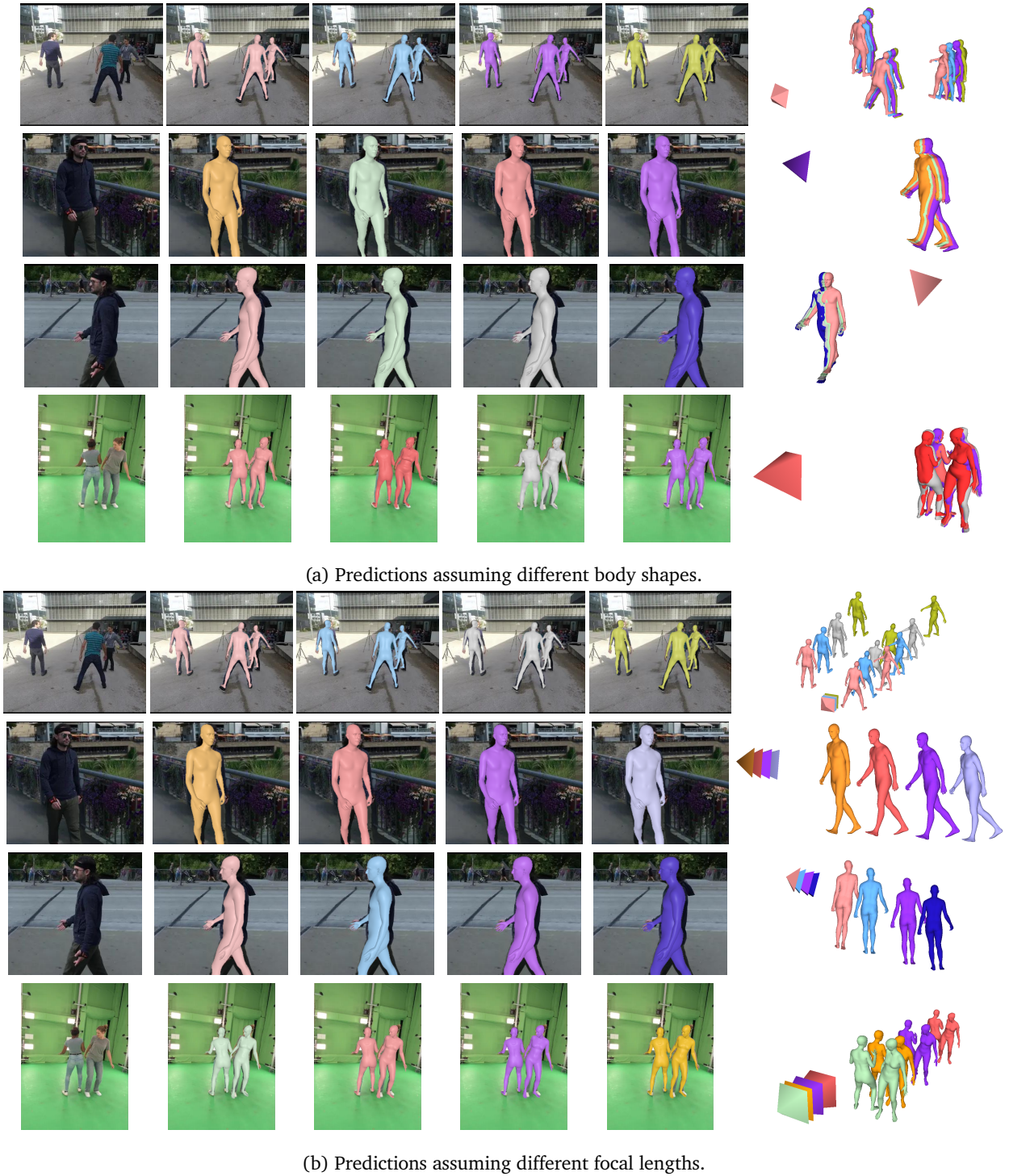
Fig. 12 illustrates the additional synthetic data generated to train our method. The images were rendered using Blender [1]. We created a collection of 3D scenes, each comprising a reconstructed indoor environment, an environment map for background and outdoor lighting, human characters, additional indoor light sources and cameras for rendering. These components were procedurally selected and combined to enhance the realism of the scenes. Specifically, we used scene meshes from Matterport3D [12], Gibson [71] and Habitat [55], along with environment maps from PolyHaven [3]. The characters were generated using HumGen3D [2], a human generator plug-in for Blender. Our synthetic data features a body shape distribution with a thicker tail than BEDLAM for increased diversity, as illustrated in Fig. 13.

#### E.2. Matching

**Matching additional inputs** To perform experiments with external body shape (*resp.* distance) inputs, we associate to each prediction the shape (*resp.* distance)

Table 3: **Quantitative evaluation** for different Bayesian network connectivity settings, with different additional inputs: camera intrinsics (*intr*), distance to the camera (*dist*), or known body shape (*shape*).

Experiments		Human3.6M			HI4D			RICH			3DPW			MuPOTS		
Ext. input	Connectivity	PVE↓	PA-PVE↓	PE↓	PVE↓	PA-PVE↓	PE↓	PVE↓	PA-PVE↓	PE↓	RJE↓	PA-RJE↓	PE↓	PCK-Matched↑	PCK-All↑	
Single-View	none	Naive-Bayes	113.6	55.3	<b>808.5</b>	92.8	47.7	168.7	119.6	<b>46.4</b>	775.3	73.9	47.9	<b>662.6</b>	84.8	73.4
		CondiMen	<b>98.9</b>	<b>54.3</b>	1145.2	<b>81.4</b>	48.0	<b>144.7</b>	<b>106.5</b>	46.6	785.1	<b>69.2</b>	<b>46.4</b>	728.9	<b>85.2</b>	74.5
		Variant1	103.9	58.4	1221.0	91.2	49.0	268.8	130.0	49.8	710.3	71.2	47.4	837.5	85.1	74.5
		Variant2	100.6	55.1	1227.8	101.5	<b>47.7</b>	182.1	127.5	46.6	<b>612.2</b>	70.2	47.0	908.2	83.9	<b>74.6</b>
	intr	Naive-Bayes	104.0	54.1	904.3	93.3	47.7	391.3	118.0	<b>46.5</b>	1060.5	73.8	47.7	428.4	84.0	72.7
		CondiMen	<b>94.3</b>	<b>53.9</b>	648.2	<b>83.0</b>	48.0	305.3	<b>106.6</b>	46.7	<b>972.3</b>	<b>69.5</b>	<b>46.4</b>	337.2	84.7	74.0
		Variant1	100.3	57.5	<b>646.8</b>	90.1	48.6	<b>286.7</b>	129.3	49.8	1029.9	71.0	47.2	<b>298.0</b>	<b>85.4</b>	<b>74.8</b>
		Variant2	95.4	54.2	682.8	101.0	<b>47.5</b>	394.5	126.1	46.5	1049.6	70.0	46.9	365.6	83.7	74.5
	intr-dist	Naive-Bayes	104.0	54.0	98.1	93.3	47.7	83.3	118.0	<b>46.4</b>	115.1	81.2	52.6	112.8	-	-
		CondiMen	<b>94.3</b>	<b>53.9</b>	89.4	<b>83.0</b>	48.0	<b>69.7</b>	<b>106.6</b>	46.7	<b>99.1</b>	76.4	51.2	104.1	-	-
		Variant1	100.8	57.4	90.1	90.1	48.6	77.6	129.7	50.0	124.4	77.5	51.5	<b>101.3</b>	-	-
		Variant2	95.4	54.2	<b>88.5</b>	100.8	<b>47.4</b>	90.7	126.1	46.6	114.8	<b>75.8</b>	<b>51.0</b>	106.3	-	-
	intr-shape	Naive-Bayes	73.6	54.1	898.0	70.9	47.3	385.0	84.2	47.9	1055.2	73.5	50.0	437.8	-	-
		CondiMen	<b>70.3</b>	<b>53.7</b>	<b>284.6</b>	<b>62.8</b>	47.6	132.2	<b>82.3</b>	<b>48.1</b>	<b>417.3</b>	<b>69.9</b>	<b>48.7</b>	354.2	-	-
		Variant1	80.2	57.4	366.2	62.9	48.2	<b>113.9</b>	87.5	51.3	508.7	72.4	49.6	<b>267.9</b>	-	-
		Variant2	72.8	54.5	676.9	65.4	<b>47.1</b>	382.0	<b>82.3</b>	48.1	1038.8	70.4	49.3	375.5	-	-
	intr-shape-dist	Naive-Bayes	73.6	54.1	56.4	70.8	47.3	59.0	84.2	<b>47.8</b>	76.8	75.9	51.0	101.6	-	-
		CondiMen	<b>70.3</b>	<b>53.7</b>	<b>56.1</b>	<b>62.8</b>	47.6	<b>46.2</b>	<b>82.3</b>	48.1	73.5	<b>72.0</b>	<b>49.6</b>	99.8	-	-
		Variant1	80.5	57.4	65.2	<b>62.8</b>	48.2	46.4	88.0	51.4	77.9	73.9	50.4	<b>97.5</b>	-	-
		Variant2	73.1	54.5	57.9	65.5	<b>47.1</b>	51.6	82.9	48.2	<b>70.2</b>	<b>72.0</b>	50.2	<b>97.5</b>	-	-
Multi-View	none	Naive-Bayes	104.8	43.8	<b>828.8</b>	85.0	<b>35.3</b>	162.2	105.8	37.1	770.5	-	-	-	-	-
		CondiMen	90.6	<b>42.6</b>	1148.3	<b>75.2</b>	35.5	<b>142.9</b>	<b>93.0</b>	<b>36.2</b>	724.5	-	-	-	-	-
		Variant1	96.0	45.3	1214.8	83.4	<b>35.3</b>	275.6	113.4	36.8	622.8	-	-	-	-	-
		Variant2	<b>88.4</b>	42.7	1240.7	94.7	<b>35.3</b>	181.8	115.4	36.5	<b>613.0</b>	-	-	-	-	-
	intr	Naive-Bayes	98.9	43.6	895.9	85.6	35.4	381.8	104.3	37.1	1057.1	-	-	-	-	-
		CondiMen	<b>88.8</b>	42.6	679.1	<b>77.0</b>	35.5	308.9	<b>92.8</b>	<b>36.2</b>	<b>903.4</b>	-	-	-	-	-
		Variant1	94.8	45.2	668.9	82.8	<b>35.3</b>	<b>281.0</b>	112.8	36.8	930.7	-	-	-	-	-
		Variant2	84.8	<b>42.4</b>	678.8	94.4	<b>35.3</b>	385.4	114.1	36.5	1050.0	-	-	-	-	-
	intr-dist	Naive-Bayes	98.9	43.6	96.8	85.5	35.4	78.7	104.3	37.1	103.4	-	-	-	-	-
		CondiMen	88.8	42.6	90.3	77.0	35.5	<b>68.8</b>	<b>92.8</b>	<b>36.2</b>	<b>89.8</b>	-	-	-	-	-
		Variant1	95.4	45.4	90.4	<b>82.9</b>	<b>35.3</b>	75.7	113.5	37.0	115.2	-	-	-	-	-
		Variant2	<b>84.9</b>	<b>42.5</b>	<b>81.6</b>	94.3	<b>35.3</b>	88.2	114.2	36.7	107.8	-	-	-	-	-
	intr-shape	Naive-Bayes	67.3	43.9	890.2	63.1	<b>34.9</b>	376.3	80.3	39.2	1053.8	-	-	-	-	-
		CondiMen	<b>62.8</b>	42.9	<b>275.0</b>	57.1	35.2	136.9	<b>77.2</b>	<b>38.6</b>	<b>439.0</b>	-	-	-	-	-
		Variant1	71.8	45.4	350.7	<b>55.8</b>	35.0	<b>116.0</b>	82.3	39.3	518.2	-	-	-	-	-
		Variant2	65.2	<b>42.8</b>	673.7	58.3	35.1	373.6	78.9	38.9	1040.2	-	-	-	-	-
	intr-shape-dist	Naive-Bayes	67.3	43.9	55.8	63.0	<b>34.9</b>	54.3	80.3	39.2	75.5	-	-	-	-	-
		CondiMen	<b>62.8</b>	<b>42.9</b>	<b>54.2</b>	57.1	35.2	45.7	<b>77.2</b>	<b>38.6</b>	74.1	-	-	-	-	-
		Variant1	72.2	45.5	62.5	<b>55.8</b>	35.1	<b>45.0</b>	83.0	39.5	80.5	-	-	-	-	-
		Variant2	65.5	<b>42.9</b>	56.5	58.7	35.1	48.4	79.7	39.1	<b>72.2</b>	-	-	-	-	-



(a) Predictions assuming different body shapes.

(b) Predictions assuming different focal lengths.

Figure 7: **Counterfactual experiments using different external inputs.** Input image (left) and predictions using different external inputs visualized from camera (middle) and side view (right).

of the closest ground truth annotation, according to the 2D distance between their reference keypoints.

**Evaluation** For evaluation, we associate each ground truth mesh with the closest prediction, according to their PA-PJE distance.

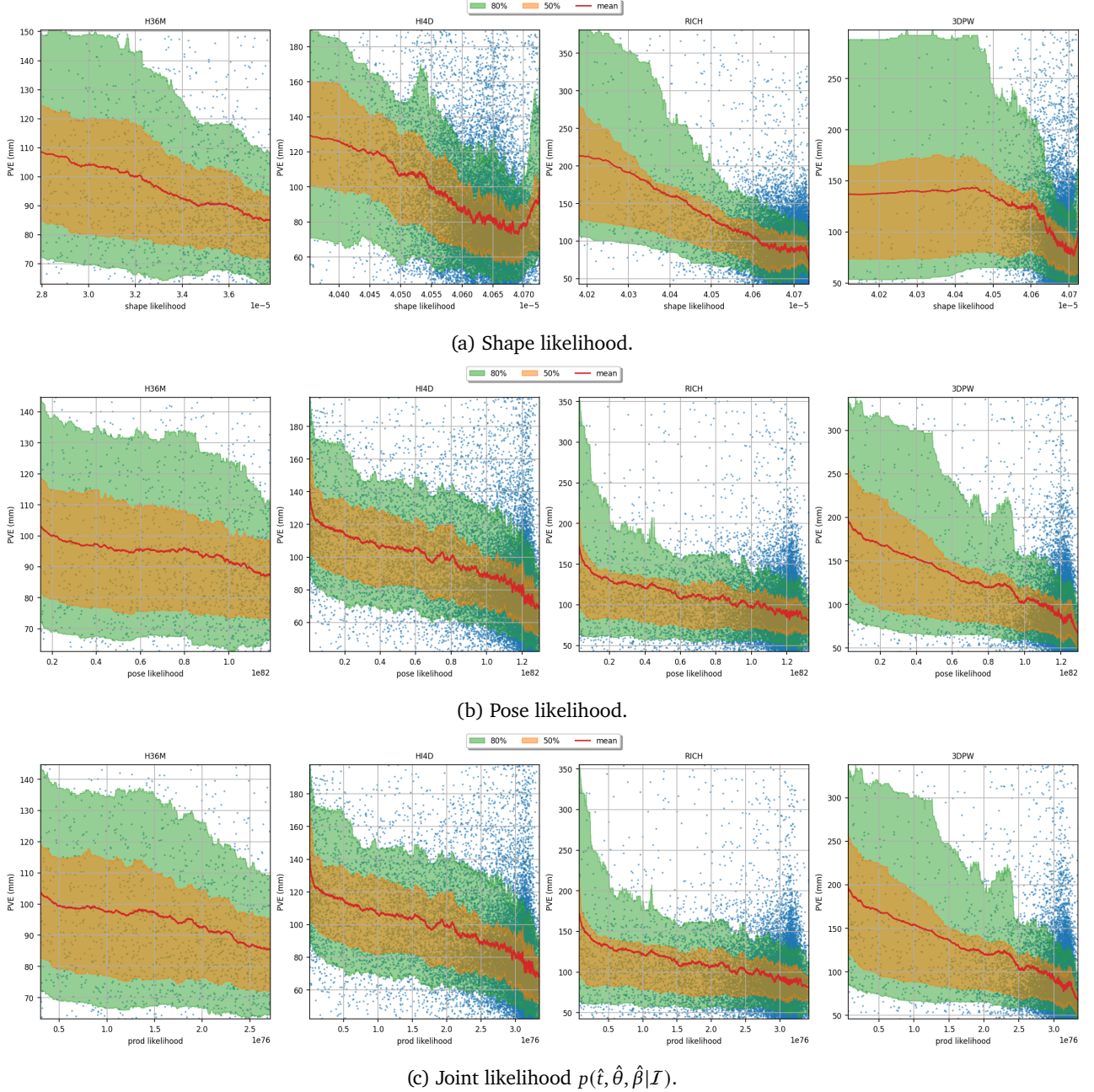


Figure 8: Relationship between prediction error and predicted likelihood across datasets. The predicted likelihood values are correlated with the test error, providing a proxy for prediction confidence. Trend curves (shown in red, yellow, and green) are calculated using a sliding window of 400 samples.



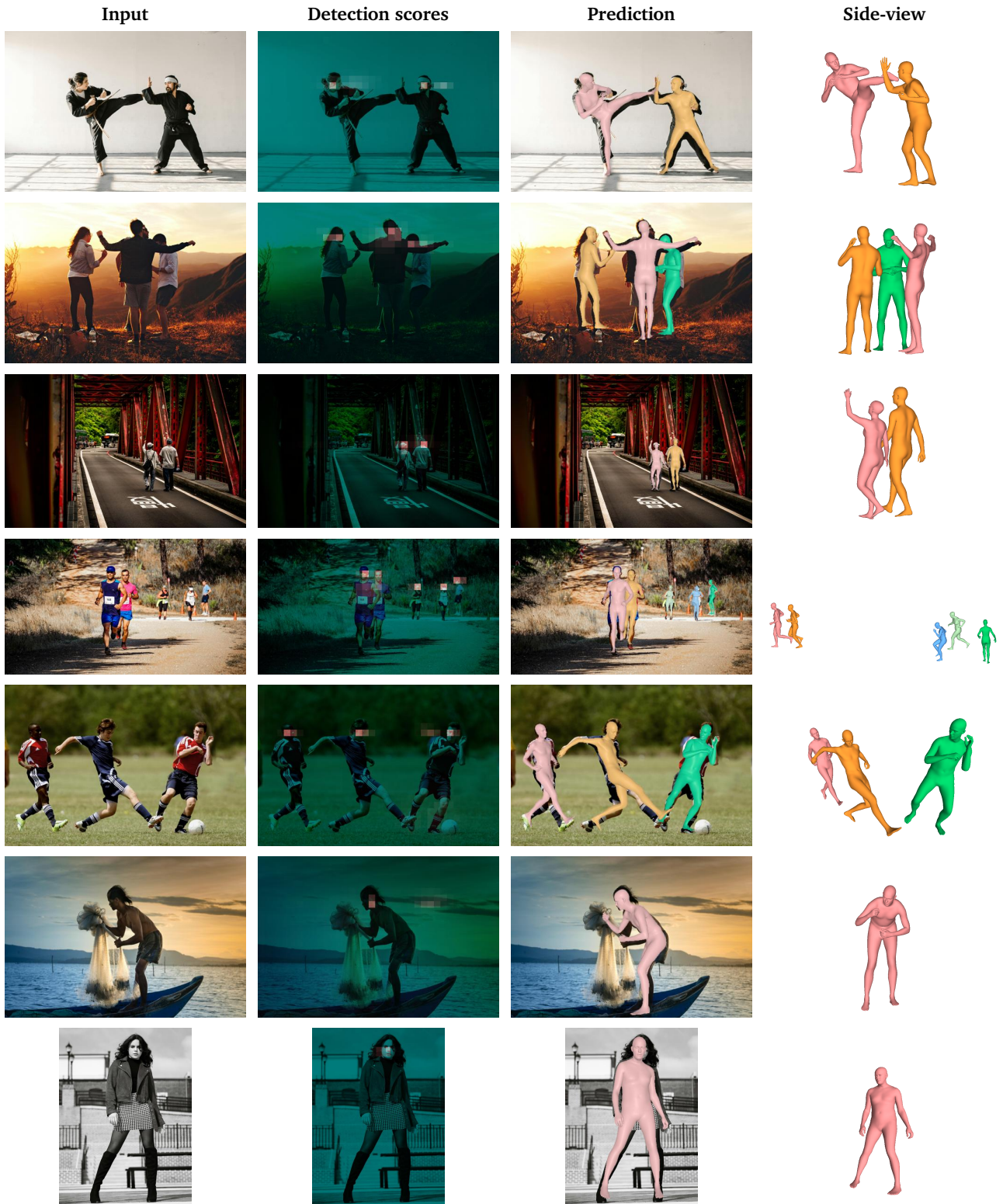


Figure 9: Qualitative examples of mesh recovery on free-to-use internet images.



Figure 10: **Limitations.** Like other existing approaches, our method struggles with unusual poses far from the training data (top row). Images depicting multiple person with reference keypoints (head) reprojecting at similar 2D locations can lead to missed detections and ambiguous predictions (bottom row).

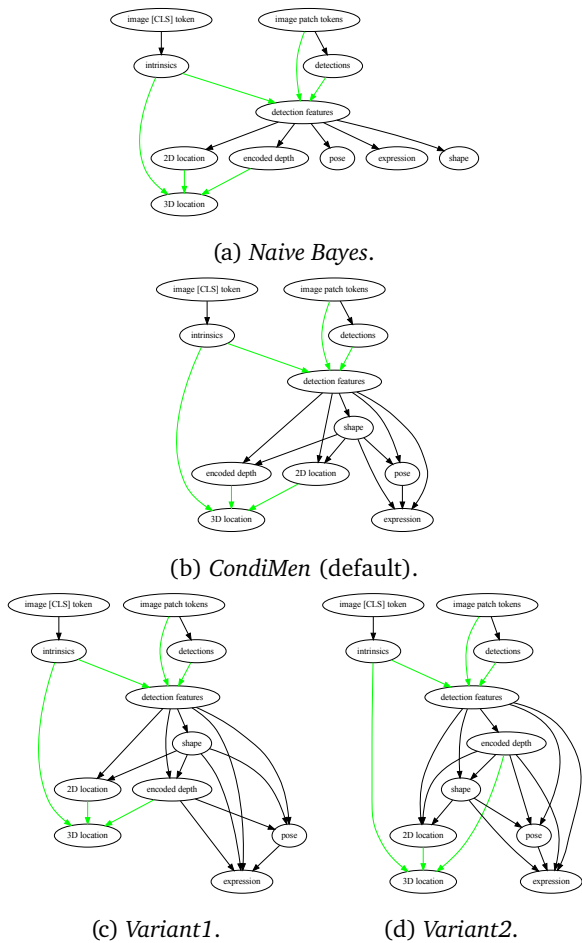


Figure 11: **Connectivity of different Bayesian networks considered for this study.** Deterministic dependencies between variables are represented in green.



Figure 12: **Examples of synthetic renderings used in our training.**

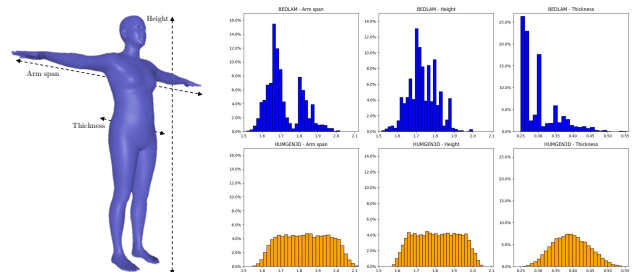


Figure 13: **Body shape statistics on BEDLAM [7] and our synthetic data.**